Check for updates

JGR Space Physics

RESEARCH ARTICLE
10.1029/2021JA029529

Key Points:

- Simulations of mesopause hydroxyl and OI layer responses to infrasonic acoustic waves driven by the 2016 M7.8 Kaikoura earthquake are performed
- Airglow perturbations from coseismic infrasonic acoustic waves replicate the progression of rupture
- Airglow observations may supplement traditional seismic data sets for future investigations of large earthquake finite-fault kinematics

Correspondence to:
P. A. Inchin,
inchinp@erau.edu

Citation:
Inchin, P. A., Guerrero, J. A., Snively, J. B., & Kaneko, Y. (2022). Simulation of infrasonic acoustic wave imprints on airglow layers during the 2016 M7.8 Kaikoura earthquake. *Journal of Geophysical Research: Space Physics*, *127*, e2021JA029529. https://doi.org/10.1029/2021JA029529

Received 19 MAY 2021
Accepted 14 FEB 2022

© 2022. American Geophysical Union. All Rights Reserved.

Simulation of Infrasonic Acoustic Wave Imprints on Airglow Layers During the 2016 M7.8 Kaikoura Earthquake

P. A. Inchin[1], J. Aguilar Guerrero[1], J. B. Snively[1], and Y. Kaneko[2]

[1]Center for Space and Atmospheric Research, Embry-Riddle Aeronautical University, Daytona Beach, FL, USA, [2]Department of Geophysics, Kyoto University, Kyoto, Japan

Abstract Simulations of hypothesized but unobserved mesopause airglow (MA) disturbances generated by infrasonic acoustic waves (IAWs) during the 2016 M7.8 Kaikoura earthquake are performed. Realistic surface displacements are calculated in a forward seismic wave propagation model and incorporated into a 3-D nonlinear compressible neutral atmosphere model as a source of IAWs at the surface-air interface. Inchin et al. (2021), https://doi.org/10.1029/2020av000260 previously showed that Global Positioning System-based total electron content (TEC) observations can be used to constrain the finite-fault kinematics of the Kaikoura earthquake. However, due to limitations of Global Navigation Satellite System network coverage and coalescence of nonlinear IAW fronts, they pointed to the relative insensitivity of the observed near-zenith TEC perturbations to the rupture evolution on the Papatea fault (PF). Here, we demonstrate that MA observations may have been able to supplement the investigation of the PF, providing information on both the timing of rupture initiation and its direction of propagation. The amplitudes of perturbations of vertically integrated volume emission rates for the simulated hydroxyl (OH)(3,1) and atomic oxygen O(^{1}S) 557.7 nm reach ∼18% peak-to-peak, and ∼3.2% (5.8 K) peak-to-peak perturbations in OH(3,1) temperature. Our results suggest that observations of nighttime MA imprints of coseismic IAWs are feasible with ground-based imagers, and may supplement the study of finite-fault kinematics of large crustal earthquakes.

1. Introduction

Inland earthquakes produce transient and permanent surface displacements that excite infrasonic acoustic waves (IAWs) in the Earth's atmosphere (Press & Harkrider, 1962). As they propagate to the upper layers of the atmosphere (∼80 km and higher), IAWs may exhibit sufficiently strong amplitudes to generat e detectable neutral and charged particle disturbances (Hines, 1960). Today, such observations facilitate the investigation of seismically generated IAW dynamics, which enable important multidisciplinary studies toward future applications (Astafyeva & Shults, 2019; Inchin, Snively, Williamson, et al., 2020; Meng et al., 2019; Savastano et al., 2017).

Recently, Inchin et al. (2021) suggested that some aspects of finite-fault kinematics of large earthquakes can be constrained from Global Navigation Satellite System (GNSS) signal-based total electron content (TEC) observations, complemented by physics-based modeling of seismic and infrasonic acoustic wave propagation and induced ionospheric plasma disturbances. The results, however, demonstrated that TEC observations of IAWs are impacted by phase canceling effects (Georges & Hooke, 1970) and, often, suboptimal geometry of line-of-sight (LOS) between GNSS satellite and receiver with respect to the spatial locations of plasma disturbances. In addition, TEC imprints of IAW dynamics occur at high altitudes from their sources (∼250–350 km). Here, IAWs are significantly impacted by thermo-viscous dissipation and a history of nonlinear effects prior to reaching the ionosphere (Inchin, Snively, Zettergren, et al., 2020; Sabatini et al., 2019). Thus, some TEC measurements may be insufficiently sensitive to IAWs to uncover temporal and spatial evolutions of earthquake rupture on individual fault segments involved in the faulting process. New observational techniques and instrumentation for the investigation of earthquake/tsunami-atmosphere coupled dynamics may provide complementary insight for these geophysical processes.

Recent modeling and observational studies show that mesopause airglow (MA) imagers can be sensitive to small-scale fluctuations, of minute periods and kilometers of wavelengths (Bittner et al., 2010; Pilger et al., 2013). Hecht et al. (2014) studied instability features and transients of less than 10 km horizontal wavelength (λ_x) seen over Maui with the Aerospace Corporation's Nightglow OH Imager of 70° field-of-view (FOV), 0.5 km horizontal resolution and 2 s of cadence time. Hannawald et al. (2016) reported observation results of small-scale transients

in hydroxyl (OH) airglow ($\lambda_x \sim 7$–10 km) with imaging system FAIM (Fast Airglow IMager) of $20 \times 24°$ FOV and horizontal resolution as fine as 120 m, acquiring two images per second. Sedlak et al. (2016) demonstrated high-resolution observations of small-scale gravity waves and turbulence features in the OH airglow with a new version of the FAIM of 17 m for pixel spatial resolution in zenith direction and FOV of 11.1×9.0 km at the OH layer height and a temporal resolution of 2.5–2.8 s. With the use of a short-wave infrared (SWIR) camera of $32 \times 27°$ FOV, 174 m of spatial resolution and 0.4 s integration time, Le Dû et al. (2020) showed that OH emissions can be disturbed by infrasound generated by ocean swells near a specific periodicity of ∼5 s. GRIPS 13 instrument (GRound-based Infrared P-branch Spectrometer), discussed in Pilger et al. (2013) and Schmidt et al. (2013), with temporal resolution of 5 s and $15 \times 15°$ FOV, were shown to capture short-period MA dynamics, including those associated with infrasound. The characteristics of these instruments may be sufficient for the detection of MA fluctuations driven by comparatively strong IAWs generated during M7–9 earthquakes.

Here, through numerical simulations, we investigate the hypothesized but unobserved MA responses to IAWs generated during the 2016 M7.8 Kaikoura earthquake to demonstrate the potential of MA observations in future seismological applications. This event is considered to be one of the most complex in-land earthquakes, with ∼20 ruptured fault segments identified from seismic and geodetic data (Hamling et al., 2017; Xu et al., 2018). The faulting area was estimated to span ∼180 km, with a rupture propagation for over ∼90 s from the hypocenter, near its southern end, to the northeast (Clark et al., 2017; Holden et al., 2017; Litchfield et al., 2018). The discrepancies in finite-fault source models among different studies led to ambiguous interpretations of the earthquake rupture evolution (Ando & Kaneko, 2018; Bai et al., 2017; Chamberlain et al., 2021; Holden et al., 2017; Ulrich et al., 2019; Wang et al., 2018). In particular, there were difficulties in isolating seismic signals generated by the Papatea Fault (PF), which is the area of large surface vertical displacements of up to ∼10 m (Tan et al., 2019; Zhang et al., 2017).

MA perturbations simulated here reach ∼18% peak-to-peak (ptp) in vertically integrated volume emission rates (IVER) of hydroxyl OH(3,1) and atomic oxygen O(^{1}S) emissions and 3.62% (5.8 K) of brightness-weighted temperature (BWT) of OH(3,1), additionally suggesting that they are potentially detectable with ground-based OH imagers, whereas O(^{1}S) 557.7 nm emission observations may capture a long-living depletion formed after the propagation of IAWs. The results show that, in comparison with TEC, the OH airglow layer is sensitive to both the timing of rupture initiation and its direction of propagation on the Papatea Fault.

2. Modeling Approach

To specify a source of seismic waves and resulting IAWs, we use a previously developed and validated earthquake source model (Inchin et al., 2021). We combined the kinematic model by Holden et al. (2017) and the specification of the Papatea Fault (PF) by Xu et al. (2018) (hereafter, Holden-Xu model) (Figure 1), that was previously found to reproduce near-epicentral seismic and geodetic observations and provide the closest agreement with detected TEC perturbations. In this model, the rupture first initiates on the Humps fault at T_0 = 11:02:56 UT, propagates predominantly to northeast on the Hundalee fault with a velocity of ∼1.9 km/s, and then moves onto the Point Kean fault offshore at $T_0 + 31$ s. Next, the rupture continues onto the northern faults, including Upper Kowhai, Kekerengu, Papatea, and Needles at a velocity of ∼2.0 km/s. Detailed description of this model can be found in Inchin et al. (2021).

To demonstrate the sensitivity of IAW imprints on the MA to the rupture evolution, we provide modeling results from simulations with various configurations of the PF, as shown in Table 1. These configurations differ in the specification of the time of rupture initiation and the direction of rupture propagation on the PF. In finite-fault Model 1, we specify rupture initiation on the PF at $T_0 + 57$ s, propagating from the south to the north, as proposed by for example, Archuleta et al. (2018), Inchin et al. (2021). In Models 2 and 3, we investigate MA responses to IAWs excited with rupture initiation on the PF at $T_0 + 27$ s (i.e., 30 s earlier than in Model 1). In Model 2 we set the same direction of rupture propagation on the PF as in Model 1–from the south to the north, while in Model 3 the direction is set from the northwest to the southeast, as proposed by Wang et al. (2018). Temporal evolution of rupture in models 1 and 2 are demonstrated in Figures 1c and 1d and the results for Model 3 are provided in https://commons.erau.edu/dm-infrasonic-acoustic-wave-imprints/. Finally, Model 4 is based on the same Holden-Xu finite-fault model, but without inclusion of the PF (Holden et al., 2017).

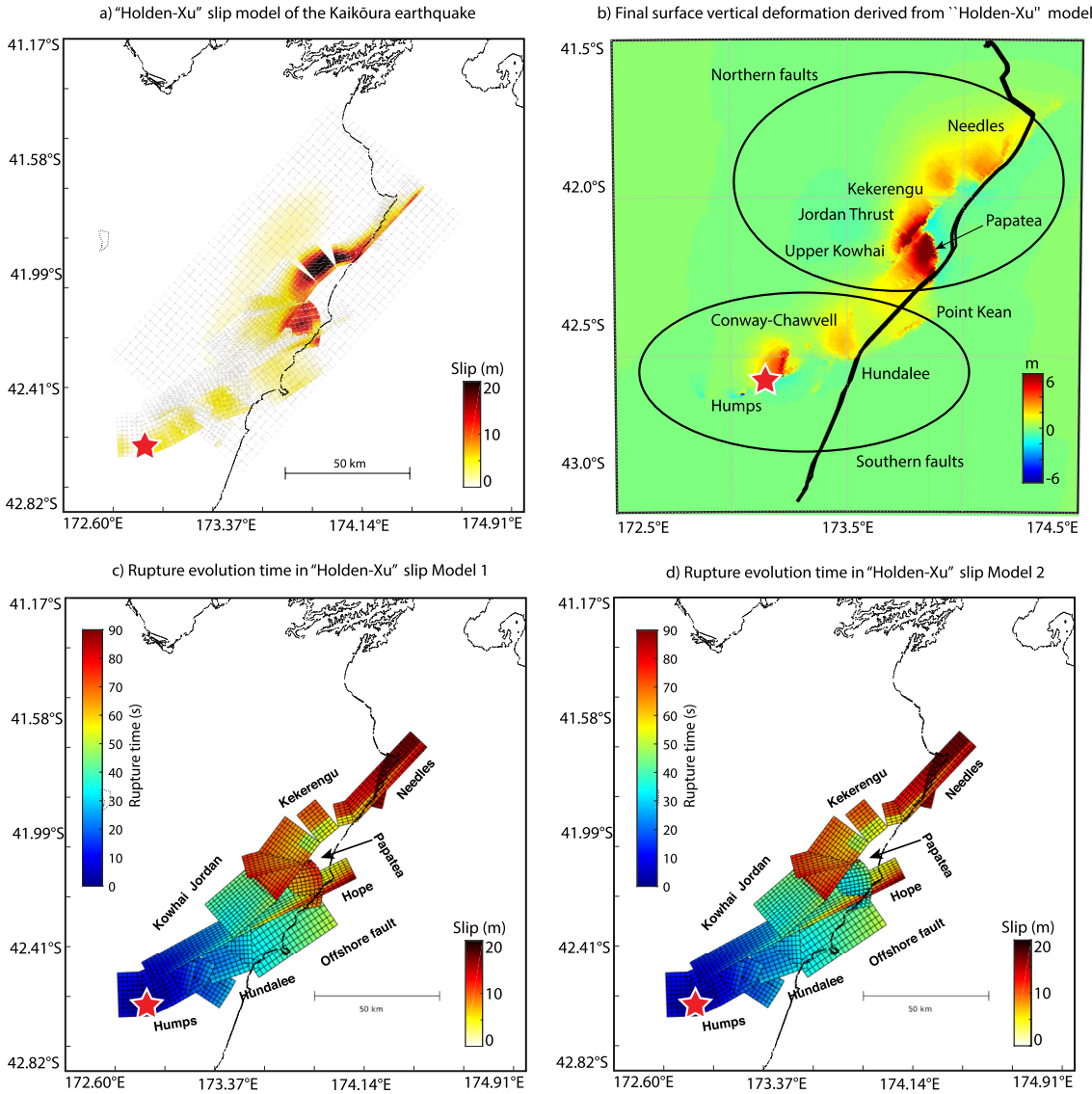

Figure 1. (a) Slip rates from the finite-fault models 1–3 (see Table 1). (b) Vertical displacement field obtained from a forward seismic wave propagation simulation based on the finite-fault model 1 with the indication of main rupturing faults and areas. The color scale on the plots is oversaturated for better visibility of small features. Temporal evolution of the rupture for (c) finite-fault Model 1 and (d) Model 2. The red star is positioned at the epicenter.

Table 1
Finite-Fault Models and Configuration of the Papatea Fault (PF)

Model	PF rupture nucleation time	PF rupture direction propagation
1. Holden-Xu	T_0 + 57 s	From south to north
2. Holden-Xu	T_0 + 27 s	From south to north
3. Holden-Xu	T_0 + 27 s	From NW to SE
4. Holden et al. (2017)	N/A	N/A

Note. T_0 = 11:02:56 UT is the origin time of the earthquake.

Surface vertical displacements, as a source of IAWs in the atmosphere, are computed using the seismic wave propagation code SPECFEM3D (Komatitsch & Tromp, 1999; Komatitsch & Vilotte, 1998). In each simulation, the surface displacements are then used to impose vertical velocity lower boundary conditions for the 3-D compressible nonlinear neutral atmosphere Model for Acoustic-Gravity wave Interactions and Coupling (MAGIC) (Snively, 2013; Zettergren & Snively, 2015). We use a 0.5 × 0.5 × 0.25 km resolution grid along latitude, longitude and altitude, respectively. A wave-absorbing (sponge) layer is applied at altitudes between 175 and 250 km, smoothly suppressing IAWs at the top of the numerical domain to avoid boundary wave reflections. The profiles of meridional and zonal winds are derived from empirical model HWM-14 (Picone et al., 2002), and temperature and major neutral species densities are derived from the empirical model NRLMSISE-00 (Drob et al., 2015).

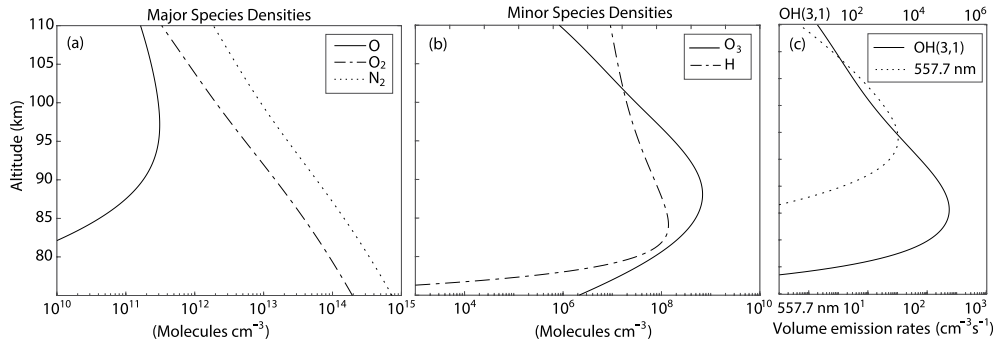

Figure 2. The profiles of initial (a) major gas (O_2, O, N_2) species densities, (b) minor gas species densities (O_3 and H), and (c) Oxygen O (^{1}S) 557.7 nm and hydroxl (OH) (3,1) ∼1504.7 nm volume emission rates used in simulations.

The configuration of MA photochemistry and dynamics is based on the formulation discussed in Snively et al. (2010) and Snively (2013), using the chemistry of Adler-Golden (1997) and Makhlouf et al. (1995, 1998). We investigate MA perturbations of two emissions: hydroxyl OH(3,1) with band center at ∼1504.7 nm and atomic oxygen O(^{1}S) at 557.7 nm. Continuity equations for ozone O_3 and hydroxyl H are solved with their chemical productions and losses, calculated time-dependently in the MAGIC simulation. The calculation of photon volume emission rates for OH(3,1) and O(^{1}S) is based on a steady-state approach, taking into account that their emission photochemistry occurs over time scales much shorter than periods of IAWs at mesospheric heights in this study. Figure 2 shows the initial profiles of major and minor gas species densities, as well as the OH(3,1) Meinel band and O(^{1}S) 557.7 nm volume emission rates incorporated into the simulations. Exponential decrease of major gas species O_2 and N_2 mass density is followed by increasing density of atomic oxygen O that plays a crucial role in the energy budgets at these heights. Two minor species (ozone O_3 and hydrogen H) dominate at altitudes 75–100 km and serve as precursors for OH production. The peak of OH(3,1) volume emission rate is at altitude ∼86 km and the peak of O(^{1}S) is at ∼95 km.

3. Simulation Results

In this section, we first demonstrate simulation results with finite-fault Model 1 in detail (Section 3.1), and then compare its results with simulations based on finite-fault models 2–4 (Section 3.2). Finally, in Section 3.3, we demonstrate synthetic images with hypothetical observation systems that may potentially capture coseismic IAWs-induced MA dynamics.

3.1. IAWs and MA Responses Simulated With Finite-Fault Model 1

The source region for IAWs in the atmosphere can be roughly divided into two areas–the southwest around Humps and Hundalee faults, and the northeast around the PF, Kekerengu and Needles faults (Figure 1b). Figure 3 presents snapshots of vertical fluid velocities at two moments of time over the heights of interest, as well as time series of vertical fluid velocities at 87 and 95 km altitudes, for positions over the southern faults (42.4°S/173.28°E) and

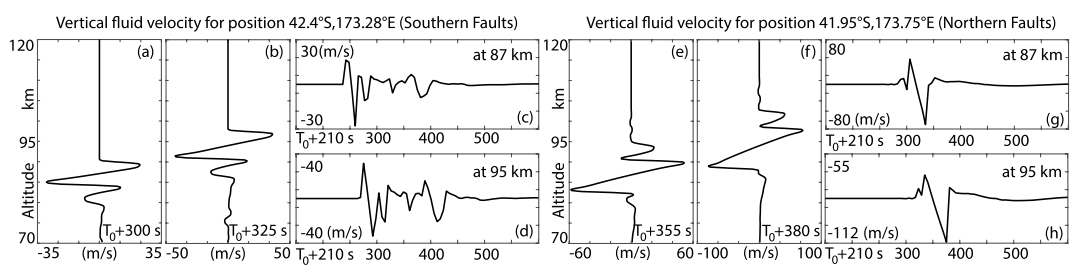

Figure 3. (a), (b), (e), and (f) Height profile of vertical fluid velocities for two positions over southern and northern faults. (c), (d), (g), and (h)Time series of vertical fluid velocities at 87 and 95 km altitudes for the same two positions over southern and northern faults. Temporal cadence of simulation output is 5 s.

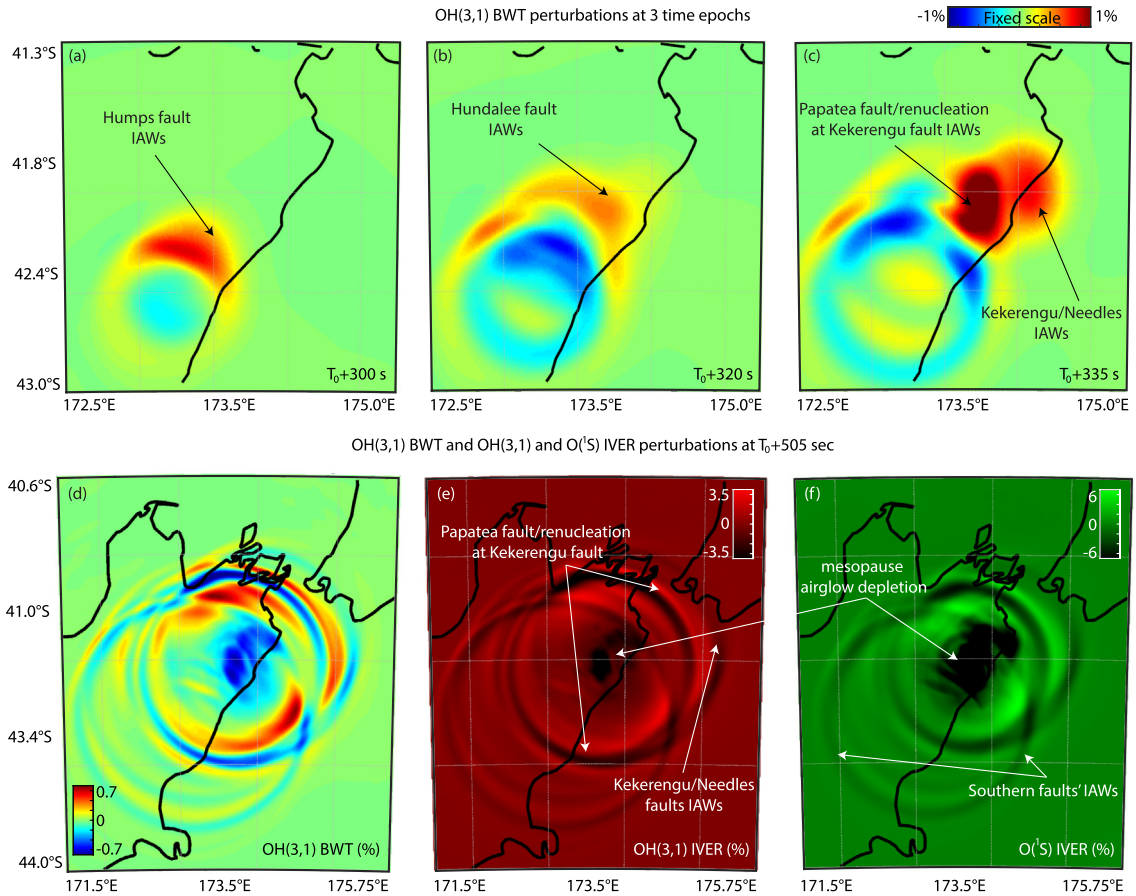

Figure 4. (a)–(c) The snapshots of Hydroxyl (OH) (3,1) brightness-weighted temperature (BWT) perturbations in percent from the background for 3 time epochs from Model 1 (Holden-Xu simulation). (d)–(f) BWT and integrated airglow photon emission rates for OH(3,1) and oxygen O (^{1}S) at T_0 + 505 s after rupture nucleation.

northern faults (41.95°S/173.75°E). The northern faults produce markedly stronger IAWs due to larger surface displacements. IAWs at mesopause altitudes already evolve to shocks and reach amplitudes −18.57/+12.73 K (−72.85/+46.96 m/s vertical fluid velocity) and −26.61/+24.73 K (−112.08/+77.09 m/s vertical fluid velocity) at 87 and 95 km respectively. Having local speeds of sound at these two altitudes of 267.68 m/s and 277.13 m/s, respectively, IAWs propagate in a strongly nonlinear regime (tens of % of local Mach number). The most discernible and the strongest acoustic shock N-wave signatures at 87–95 km heights, formed over southern and northern fault areas, exhibit periods of ∼30–45 s and the propagation of the overall packet of individual shocks takes ∼2 min. These shock N-waves have vertical wavelengths of 7–11 km at these heights, thus being comparable or larger than the depth of the full layer of OH or O(^{1}S). The IAWs generated by transient displacements from seismic wave propagation farther from the epicentral area, are comparatively weak and exhibit amplitudes of ∼3 K and ∼14 m/s of vertical fluid velocities. The link, https://commons.erau.edu/dm-infrasonic-acoustic-wave-imprints/ includes the data sets of vertical fluid velocity fields for the moments of time presented in Figure 3. We also refer to Inchin et al. (2021) who discussed simulation results of IAW evolution from ground level to the ionosphere with the use of the same finite-fault models in detail.

The temporal and spatial evolution of perturbations simulated with the finite-fault Model 1 MA disturbances closely replicate the propagation of the rupture–from the southwest to the northeast. Figures 4a–4c presents OH(3,1) BWT perturbations at three time epochs. The earliest arrival of IAWs to mesopause heights occurs at T_0 + 240 s (see the animation in https://commons.erau.edu/dm-infrasonic-acoustic-wave-imprints/), what is roughly consistent with the time of acoustic wave arrival from the ground to the altitudes of the OH(3,1) layer (Figure 4a). MA disturbances are focused to the northeast and result from IAWs generated during the rupture propagation on the Humps fault from the southwest to the northeast. Over Humps fault, OH(3,1) BWT perturbations reach ∼1.12% (∼2 K), and 4.9% and 4% ptp for OH(3,1) and O(^{1}S) IVER, respectively. Demonstrated in this section

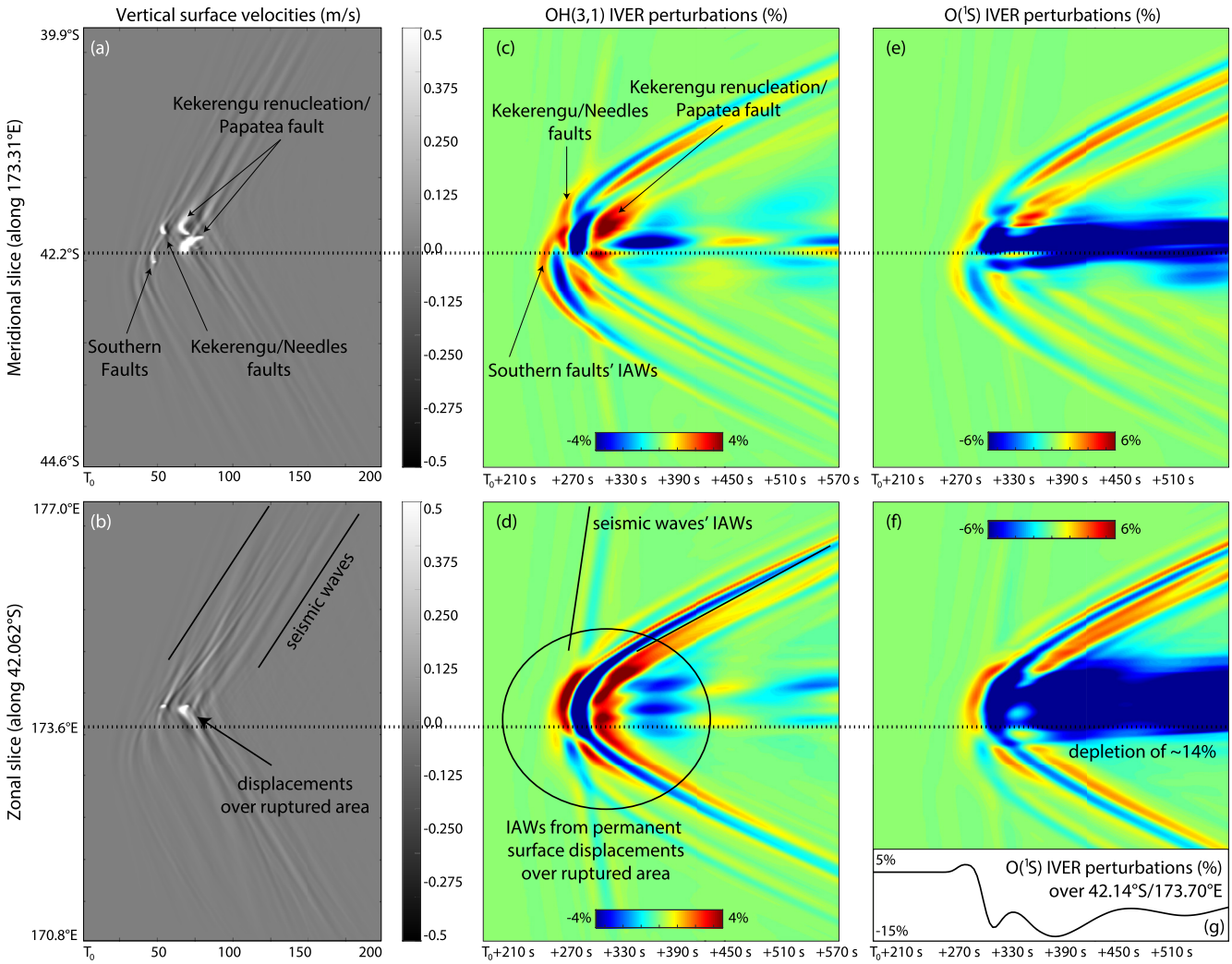

Figure 5. Latitude-time diagrams of (a), (b) surface vertical velocities, (c), (d) OH(3,1), and (e), (f) O(^{1}S) integrated volume emission rates (IVER) perturbations for meridional (top) and zonal (bottom) slices. The plots are oversaturated for better visibility of weak signatures. (g) Time series of O(^{1}S) IVER perturbations over 42.14°S/173.70°E. Note that time labels in panels (c)–(g) starts at $T_0 + 210$ s.

IVER is calculated by integrating volume emission rates vertically for each horizontal position of the numerical domain. At later time, MA perturbations of ~1.24% OH(3,1) BWT (~2.2 K), ~7.2% ptp OH(3,1), and 9.3% ptp O(^{1}S) IVER appear east-northeast, and are linked with IAWs that are excited when the rupture propagates on the Hundalee and Point Kean faults (Figure 4b).

Next, the MA perturbations appear over northern faults. The strongest perturbations (~3.2% ptp OH(3,1) BWT (~5.8 K ptp), ~18% ptp OH(3,1), and O(^{1}S) IVER) appear over the PF and rupture reactivation at the southern end of the Kekerengu fault (Figure 4c). Here, MA layers experience steep and nonlinear displacements driven by strongly nonlinear IAWs, followed by quasi-permanent emission depletions apparent in O(^{1}S) volume emission rates. These perturbations overlay upon those appearing farther north-northeast and attributable to the rupturing on the northern part of Kekerengu and Needles faults (Figure 4c). We additionally present the OH(3,1) BWT, OH(3,1), and O(^{1}S) IVER perturbations at $T_0 + 505$ s in Figures 4d–4f. Horizontally expanding IAWs drive detectable perturbations of ~3%–7% ptp OH(3,1) and O(^{1}S) IVER. Even at this later time epoch, the southern and northern fault areas of IAW generation can be distinguished in MA emissions.

Figure 5 presents time-distance diagrams of vertical surface velocities and OH(3,1) and O(^{1}S) IVER perturbations for meridional (along 173.31°E) and zonal (along 42.062°S) slices. As expected, the strongest MA perturbations are generated from permanent surface displacements over the ruptured area. Away from the epicentral area, MA

perturbations with apparent horizontal phase velocities of ~3.5 km/s are driven by IAWs from seismic wave propagation, but they are fairly weak (<1% OH(3,1) IVER). First MA perturbations appear above the southern faults and then shift to the northern fault area, and practically mimic the evolution of ground displacements (Figures 5c and 5d). From these diagrams, it is difficult to discern MA perturbations driven by the PF and the Kekerengu fault separately, as their displacements produce IAWs over a spatially localized region practically simultaneously. After the propagation of IAWs, OH(3,1) IVER continues fluctuating and damping, but O(^{1}S) IVER is locally depleted by ~12%–14% due to nonlinear responses of this layer to strongly nonlinear IAWs (Figures 5e–5g).

3.2. Comparison of MA Responses to IAWs Simulated With Finite-Fault Models 1–4

The determination of rupture initiation time and rupture propagation direction on the PF using conventional seismic and geodetic data sets is complicated due to the difficulty of the retrieving of PF signals from available sparse seismic observations (Holden et al., 2017). Here, we demonstrate that MA fluctuations, generated by IAWs, closely replicate the rupture evolution on the PF.

The snapshots of MA perturbations from 3 simulations with finite-fault models 1–3 are presented in Figure 6. For each simulation, OH(3,1) IVER, and BWT perturbations at T_0 + 300 s and O(^{1}S) IVER at T_0 + 340 s are provided. In the simulation with Model 1, due to the later time of rupture initiation on the PF (T_0 + 57 s), IAWs excited above the PF and northern faults do not yet reach 80–95 km altitudes, and thus, at the time epoch shown, MA perturbations are generated only by the southern faults (Figure 6a–6c). In comparison, from simulation results with finite-fault Models 2 and 3, which include PF rupture initiation at T_0 + 27 s, MA perturbations generated by the PF are already seen at these time epochs (Figure 6d–6i).

Next, we demonstrate simulation results of MA perturbations from simulations with models 1–3 for OH(3,1) at T_0 + 320 s and O(^{1}S) at T_0 + 360 s in Figure 7. The propagation of the rupture on the PF from the south to the north, as specified in Model 2, are causes for the focusing of IAWs and related MA perturbations to the northeast (Figures 7d–7f). In contrast, the propagation of the rupture on the PF from the northwest to the southeast, results in focusing on IAWs and MA perturbations to the southwest (Figures 7g–7i). Although the focusing of IAWs is constrained in the southwest-northeast direction, and this is connected with the spatial orientation of the PF and respective vertical surface displacements, MA imprints still demonstrate the sensitivity to the variation in the direction of rupture propagation on the PF.

Finally, we demonstrate the time series of maximum absolute ptp OH(3,1) IVER perturbations from simulations with finite-fault models 1–4 in Figure 8. The link, https://commons.erau.edu/dm-infrasonic-acoustic-wave-imprints/ includes the table of values of OH(3,1) IVER perturbations presented on a plot, as well as of OH(3,1) BWT (absolute and percent from the background) and O(^{1}S) IVER. Earlier initiation of the rupture on the Papatea Fault in simulations with models 2 and 3 leads to earlier appearance of OH(3,1) IVER perturbations than in the simulation with Model 1. The peaks highlighted in the oval demonstrate compression (9%–10.5% OH(3,1) IVER) and rarefaction phases (~14%–16% OH(3,1) IVER) of IAW propagating through the OH layer. Stronger perturbations in the simulation with Model 3 (than in the simulation with Model 2) result from constructive interference of IAWs from the southern faults and focused to the southwest IAWs excited over the Papatea Fault. The peak of perturbations in all simulations at T_0 + 370 s is linked with the depletion generated after the propagation of the IAWs. At the same time, the absence of the Papatea Fault in the simulation with finite-fault Model 4 leads to the weakest perturbations (~12% OH(3,1) and O(^{1}S) IVER, 2.38% OH(3,1) BWT or 4.28 K). Such comparative analysis of peak amplitudes of MA emission perturbations may provide hints on the dynamics of IAWs and thus their sources along the whole spatial and temporal extent of the earthquake rupture.

3.3. Simulation of MA Observation Systems

The simulation results suggest that a moderate earthquake, such as the Kaikoura earthquake in New Zealand in 2016, can drive IAWs of amplitudes of tens of Kelvins and periods of 30–45 s at mesopause altitudes, with corresponding wavelengths of 7–11 km. IAWs may result in OH(3,1) IVER fluctuations of ~15%–18% and OH BWT of up to ~5.8 K. O(^{1}S) IVER fluctuations reach ~18%, and exhibit a persistent depletion of the emission.

To demonstrate the potential to capture such dynamics in MA, we simulate several observation systems. The characteristics of simulated imagers are presented in Table 2. FOV is the solid angle that represents the imager's

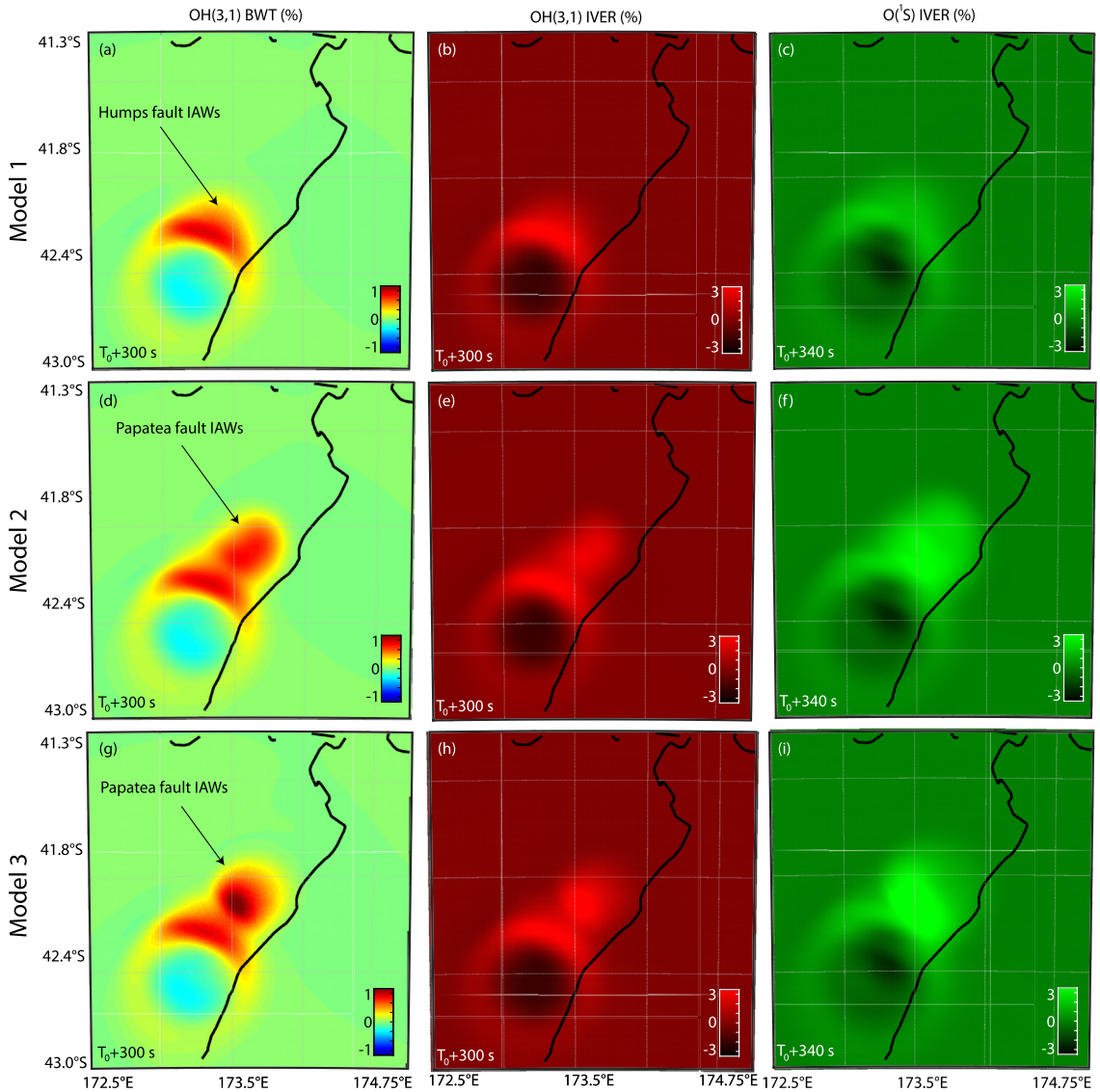

Figure 6. Snapshots of perturbations in the hydroxyl (OH) (3,1) brightness-weighted temperature (BWT; left column), the OH(3,1) integrated volume emission rates (IVER; middle column), and oxygen O (^{1}S) IVER (right column) from 3 simulations with finite-fault models 1–3 introduced in Table 1. The snapshots in the right column are provided at a later moment of time due to later arrival of infrasonic acoustic waves at O(^{1}S) heights.

view; it is expressed in terms of the radially symmetric planar viewing angle with the imager's zenith at the center. We first simulate a narrow FOV (40°), but high temporal resolution imager with an integration time $\lesssim$1 s. This assumption of a short integration time $\lesssim$1 s is made on the basis that it is notably shorter than the resolvable IAW time-scales of the simulation, in terms of effective model resolution and sampling. The second OH(3,1) observation system has a FOV of 70° and an integration time of 5 s. Finally, we simulate 100° FOV OH(3,1) imager with an integration time of 10 s, similar to the system discussed by Pautet et al. (2014). For the O(^{1}S) we simulate observation systems with 20 and 30 s integration times and 70° and 100° FOV, respectively. Each imager has the same number of pixels–256 × 256. The resolution in Table 2 is reported at zenith direction, whereas it degrades with increasing angle of observations, for example, at 45° zenith angle it may be reduced by half. The animations of images with all 5 observation systems and their unwarped representation on geographical maps are provided in https://commons.erau.edu/dm-infrasonic-acoustic-wave-imprints/.

The images of OH(3,1) and O(^{1}S) IVER are synthesized by the integration of three-dimensional simulated airglow layer volume emission rates along the line-of-sight (LOS) for each pixel in a 256 × 256 array. An imager is represented by its lens profile and FOV, being at particular location and rotated, pointing at specified tilt and

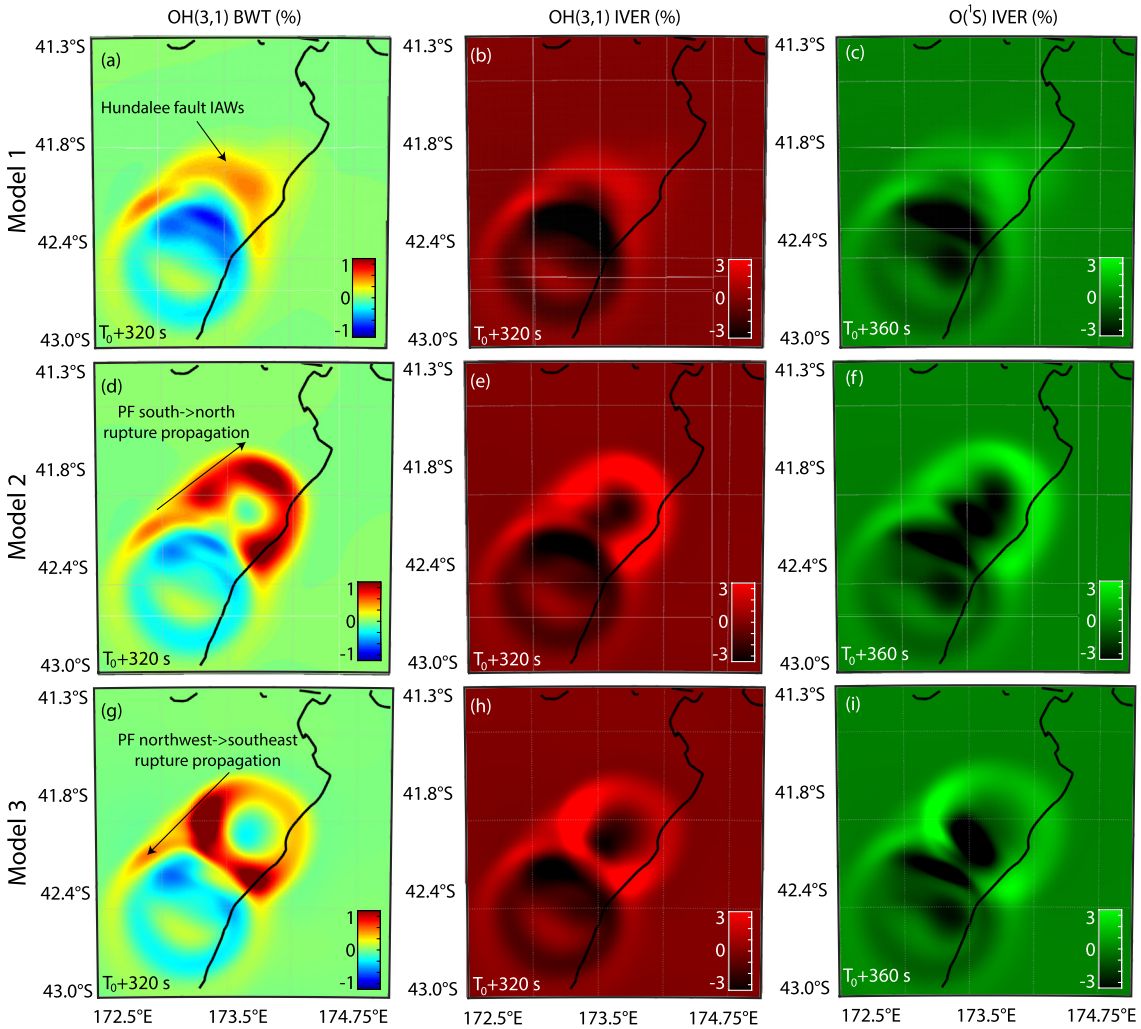

Figure 7. Snapshots of perturbations in the hydroxl (OH) (3,1) brightness-weighted temperature(BWT; left row), the OH(3,1) integrated volume emission rates (IVER; middle column), and O(^{1}S) IVER (right column) from 3 simulations with finite-fault models 1–3 introduced in Table 1. Time epochs of the snapshots are indicated in each panel. The plots are oversaturated for better visibility of weak signatures. The snapshots in the right column are provided at a later moment of time due to later arrival of infrasonic acoustic waves at oxygen O (^{1}S) heights.

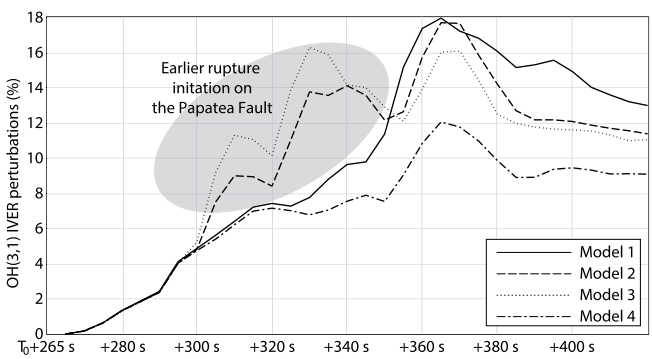

Figure 8. Absolute maximum ptp hydroxl (OH) (3,1) integrated volume emission rates (IVER) perturbations at each moment of time for the whole numerical domain from simulations with finite-fault models 1–4.

azimuth angles. We find the intersection of each pixel's LOS and an ellipsoid that represents an atmospheric layer at each height. Each of these ellipsoids are obtained by expanding the semi-major axis of the WGS84 reference ellipsoid by every increment along the LOS. The semiminor axis is calculated with the original flattening of the WGS84 ellipsoid, thus preserving its shape at every height. The spatial resolution along LOS (for the integration of emission volume rates) is set as 125 m. With this mapping we interpolate the volumetric data at every intersection point and then integrate along the LOS to obtain a flat image. This effectively maps a thick airglow layer onto a 2-D pixel surface, such as a CCD or solid-state sensor. This is done for both perturbation and background data to obtain relative perturbations. The resulting synthetic image is then unwarped at the VER peak heights of OH(3,1) and O(^{1}S) layers by using the same LOS-ellipsoid intersection algorithm, at 87 and 95 km altitudes, respectively. The integration time is incorporated by integrating data sets from synthetic images in the related time window and dividing the results by the number of frames.

Table 2
Characteristics of Modeled Imagers

Imager	Emission	Field-of-view (FOV)	Resolution per pixel (zenith)	Integration time (IT)
1.	OH(3,1) ~1504.7 nm	40°	237 m	$\lesssim$1 s[a]
2.	OH(3,1) ~1504.7 nm	70°	415 m	5 s
3.	OH(3,1) ~1504.7 nm	100°	593 m	10 s
4.	O(^{1}S) 557.7 nm	70°	453 m	15 s
5.	O(^{1}S) 557.7 nm	100°	647 m	30 s

[a]Shorter than the resolvable infrasonic acoustic wave time-scales of the simulation.

First, we demonstrate images captured with zenith-looking observation systems in Figure 9. We use the center of the numerical domain as the location of imagers (42.198°S/173.653°E). The images with observation system 1, presented in Figures 9a–9e, demonstrate that even a comparatively narrow FOV imager could be sufficient to detect OH(3,1) VER fluctuations driven by the southern faults (Figures 9a and 9b), and strong fluctuations driven by the PF and the southern part of the Kekerengu fault (Figure 9c). Images with observation systems 2 and 3 in panels f–o also demonstrate that short integration times of 5 and 10 s lead to only slightly blurred, but still discernible dynamics of IAWs from the southern and northern faults. In comparison, images with observation system 5 demonstrate that a long integration time (here, 30 s) leads to substantial smoothing of the MA dynamics. Nevertheless, even with such long integration time, it is possible to discern fluctuations and especially those connected with emission depletion.

Next, in Figure 10, we demonstrate synthetic images with observation system 2 from Table 2, varying its location and camera azimuth angle. Tilt of the camera (zenith angle) is set as 35° in all three scenarios shown. Imager locations and geometry of observations relative to MA dynamics lead to highlighting of various parts of MA fluctuations due to phase canceling effects. All 3 setups of imagers would be useful in discerning the dynamics of interest, highlighting the evolution of the IAWs (and thus rupture evolution) from the southwest to the northeast, with the strongest fluctuations over the PF.

4. Discussion and Conclusion

We have investigated the characteristics and evolution of mesopause airglow (MA) perturbations generated by infrasonic acoustic waves (IAWs), excited during the 2016 M7.8 Kaikoura earthquake. We first calculated realistic time-dependent surface displacements in forward seismic wave propagation simulations. Then, vertical surface velocities were used at the bottom boundary condition in the 3D nonlinear neutral atmosphere model MAGIC for the simulation of IAWs, along with their observable effects on the MA photochemistry.

The variations of OH(3,1) and O(^{1}S) IVER perturbation amplitudes are in the range 6%–18% from the background states (or 1–5.8 K of OH(3,1) BWT, 0.6%–3.2% from the background state) over different regions of the ruptured area. The nonlinear response of the O(^{1}S) layer leads to the formation of a mesopause airglow depletion of ~12%–14%. The scales of resulting perturbations closely match those of IAWs and are in the range 30–45 s period pulse durations for the dominant acoustic N-wave shocks with 7–11 km wavelengths at mesopause altitudes. The IAWs themselves experience strongly nonlinear evolutions having amplitudes of tens of % of local Mach number (~260–280 m/s of vertical fluid velocities). The amplitudes of MA perturbations generated by distant seismic waves (e.g., Rayleigh waves), in contrast to those generated in the near-epicentral region, are fairly small and are unlikely to be registered with modern imagers.

Modeling results further support that MA observations may supplement the investigation of finite-fault kinematics of large earthquakes at nighttime. Simulated MA perturbations include information on both the time of rupture initiation and the direction of rupture propagation on the PF. The absence of the PF IAW source processes results in ~26% weaker OH(3,1) BWT perturbations (4.3 vs. 5.8 K of OH(3,1) BWT perturbations). Interestingly to note, Inchin et al. (2021) found a similar relative difference in amplitudes of TEC perturbations from simulations with and without the PF.

We explored and addressed the possibility to infer earthquake rupture evolution from IAW imprints on MA in 4 specifications of the PF, based on earlier published assumptions about it (e.g., Archuleta et al., 2018; Holden et al., 2017; Inchin et al., 2021; Wang et al., 2018). The detection and analysis of such short-period MA transients could potentially be achieved with modern OH imagers of high temporal and spatial resolutions (Hannawald et al., 2016; Hecht et al., 2014; Pautet et al., 2014; Sedlak et al., 2016), whereas current O(^{1}S) imagers may be suitable for the detection of the depletion in emissions resulting from the propagation of strong nonlinear acoustic shock waves. Such observations may be useful in regions of sparse networks of seismic and geodetic observations and in cases of complex, multi-fault earthquakes. They may also be used to study undersea earthquakes, as

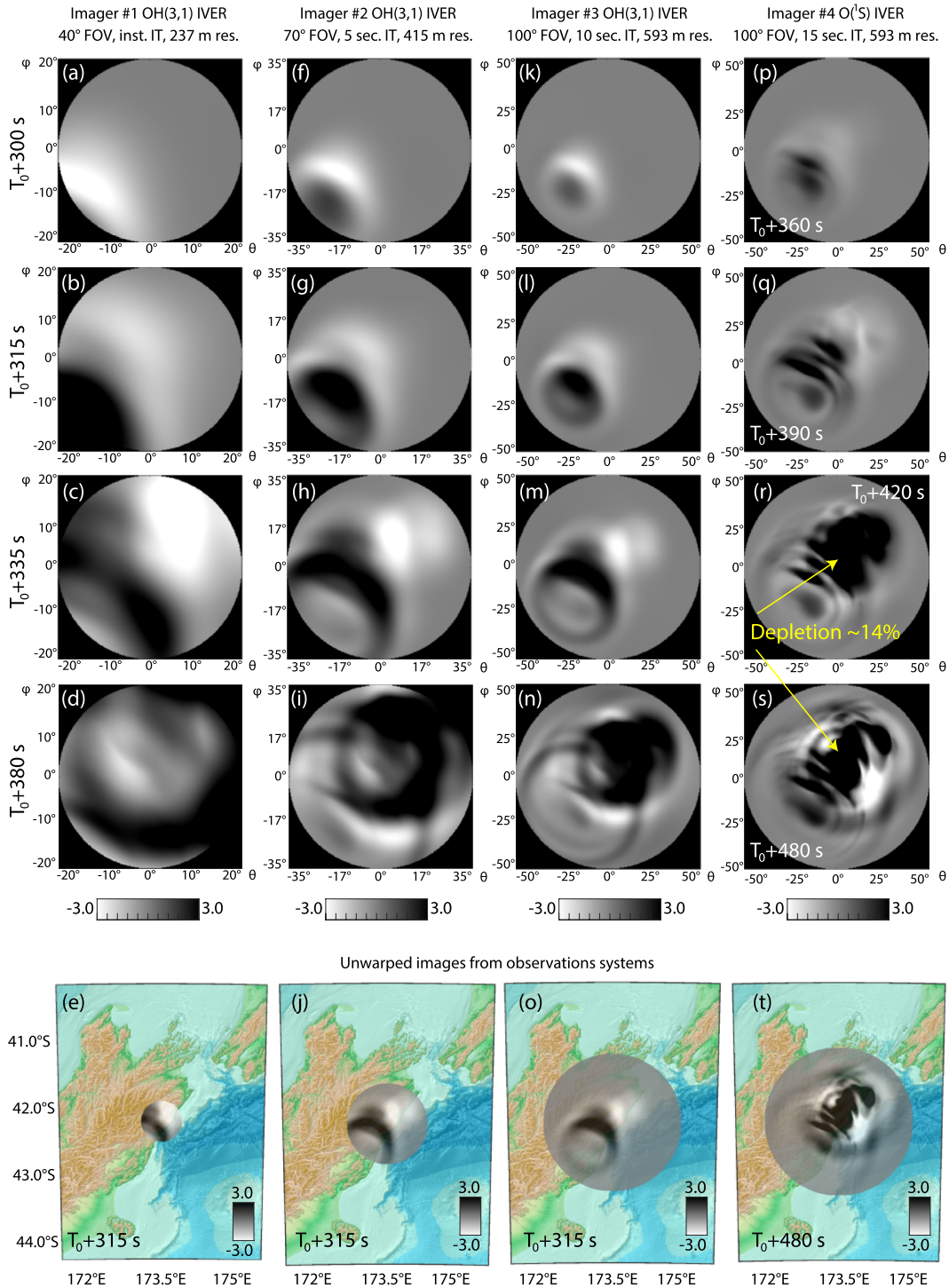

Figure 9. Synthetic images of integrated volume emission rates (IVER) for the observation systems presented in Table 2 and their unwarped representations on a geographic map. The images are shown on an oversaturated scale for visibility of weaker features. An opacity is added to the unwarped images to visualize the underlying topography. Time epochs of snapshots for oxygen O (^{1}S) IVER are specified separately.

a source of information on ocean surface displacements and their evolution, potentially useful for the estimation of tsunami hazard. We highlight that MA observations may not uncover other rupture progression configurations, for example, shorter time difference of rupture initiation on the Papatea fault between models. Further parametric

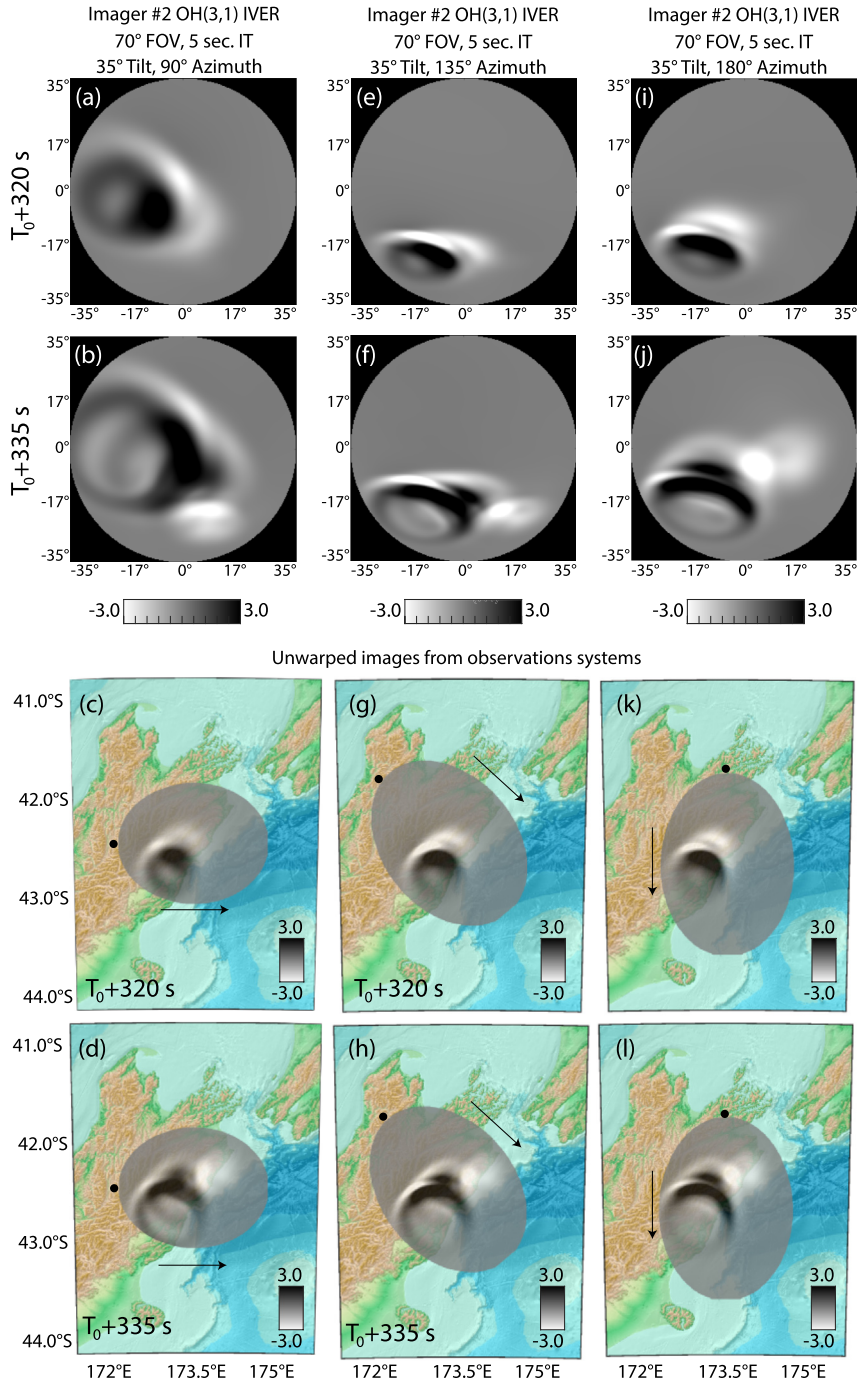

Figure 10. Synthetic images of integrated volume emission rates (IVER) captured with observation systems 2 with different azimuth angles and location of the imager and its unwarped representations on a geographic map. Black dots depict the position of imagers and arrows–directions of pointing.

modeling and observational campaigns may be directed toward the investigations of MA sensitivity to a broad range of rupture evolutions.

Earlier, based on modeling results, Inchin, Snively, Williamson, et al. (2020) demonstrated that strongly nonlinear IAWs can drive potentially detectable MA perturbations over epicentral regions of large crustal earthquakes. At the same time, the simulated IAWs and MA responses could be uncommonly large due to unprecedentedly large displacements produced by the 2011 M9.1 Tohoku-oki earthquake. Here, along with the investigation of

the information that MA observations of IAWs may provide on related surface dynamics, we demonstrated that earthquakes of magnitude 7–8, which occur more frequently, may also result in comparatively large fluctuations in MA, up to ∼18% in OH(3,1) and O(^{1}S).

The displacements of emitting particles considered here are aligned with the transport of major and minor neutral species, thus providing direct information on IAW dynamics, in comparison with TEC observations which include plasma responses to IAWs affected by magnetic field effects. The results demonstrate that IAWs at 85–105 km include more comprehensive information about their source, whereas individual shocks at ∼200 km upward (at altitudes where TEC perturbations are detected) fully coalesce into shock N-waves and experience substantial smoothing due to thermo-viscous dissipation (Inchin et al., 2021). Also, MA observations can provide data sets several minutes earlier than TEC observations in tsunami early warning system applications. However, these measurements still depend on the mutual geometry between the LOS and the direction of motion of the emitting particles. Practically, the requirement for nighttime operation, without clouds or a bright Moon, of the airglow imaging systems synthesized here is a main drawback, whereas perturbations in TEC can be studied at any time of the day.

We caution that several factors may affect the agreement of simulation results with MA observations of coseismic IAWs. The biases in the determination of background atmospheric state (e.g., temperature, neutral species densities, and kinematic viscosity) and wind profiles from empirical models, such as NRLMSISE-00 and HWM14 used here (Drob et al., 2015; Picone et al., 2002), may cause differences in the determination of IAW amplitudes and their arrival times at mesopause altitudes. In addition, as MA observations present integrated values, the determination of the exact time of arrival of leading IAW shocks is complex. We also defer diagnosing the duration of the mesopause airglow depletion's ("hole") recovery following impact of a nonlinear IAW, but it is important to note that even for the Kaikoura earthquake of magnitude 7.8, the MA hole can be formed and likely observed to persist. A more detailed description of airglow dynamics and chemistry, along with the incorporation of long-period and large scale planetary, tidal, turbulence and wind dynamics can provide additional insight and fidelity in simulations. To understand thresholds of detectability and sensitivities to atmospheric parameters, parametric studies will also be of considerable value, and are now pending.

The practical detection of fluctuations associated with nonlinear IAWs in MA would require imagers specifically configured or adapted to investigate the dynamics of interest, but this discussion is beyond the scope of the current manuscript. Nevertheless, the model simulation results strongly suggest that imaging of the MA IAW fields associated with the 2016 Kaikoura earthquake may have helped to clarify hypotheses on the PF rupture process and timing, thus warranting further investigation.

Data Availability Statement

SPECFEM3D-Cartesian codes are available through https://geodynamics.org/. The geographic map used for unwarped images in Figure 9 is taken from General Bathymetric Chart of the Oceans (GEBCO) archive (https://download.gebco.net/). Detailed movies of the simulations and relevant data in support of reproducibility can be found here: https://commons.erau.edu/dm-infrasonic-acoustic-wave-imprints/.

Acknowledgments
This research was supported by NASA grants 80NSSC18K1037 and 80NSSC20K0495 to ERAU, a Rutherford Discovery Fellowship provided by the Royal Society of New Zealand, and DARPA Cooperative Agreement HR00112120003. This work is approved for public release; distribution is unlimited. The content of the information does not necessarily reflect the position or the policy of the Government, and no official endorsement should be inferred. We thank Ian Hamling for providing us the vertical displacement field derived from SAR azimuth and range offsets. The authors gratefully acknowledge the use of the ERAU Vega High-Performance Computing Cluster and New Zealand's NeSI Computing Cluster.

References

Adler-Golden, S. (1997). Kinetic parameters for oh nightglow modeling consistent with recent laboratory measurements. *Journal of Geophysical Research*, *102*(A9), 19969–19976. https://doi.org/10.1029/97JA01622

Ando, R., & Kaneko, Y. (2018). Dynamic rupture simulation reproduces spontaneous multifault rupture and arrest during the 2016 mw 7.9 kaikoura earthquake. *Geophysical Research Letters*, *45*(23), 12875–88312. https://doi.org/10.1029/2018GL080550

Archuleta, R. J., Ji, C., & Adams, M. N. (2018). Strong ground motion from earthquakes with multiple faults. *SMIP18 Seminar on Utilization of Strong-Motion Data Proceedings*, *10*, 1–15. https://www.conservation.ca.gov/cgs/Documents/Program-SMIP/Seminar/SMIP18_P1_Paper%20by%20Archuleta.pdf

Astafyeva, E., & Shults, K. (2019). Ionospheric gnss imagery of seismic source: Possibilities, difficulties, and challenges. *Journal of Geophysical Research: Space Physics*, *124*(1), 534–543. https://doi.org/10.1029/2018JA026107

Bai, Y., Lay, T., Cheung, K. F., & Ye, L. (2017). Two regions of seafloor deformation generated the tsunami for the 13 November 2016, Kaikoura, New Zealand earthquake. *Geophysical Research Letters*, *44*(13), 6597–6606. https://doi.org/10.1002/2017GL073717

Bittner, M., Höppner, K., Pilger, C., & Schmidt, C. (2010). Mesopause temperature perturbations caused by infrasonic waves as a potential indicator for the detection of tsunamis and other geo-hazards. *Natural Hazards and Earth System Sciences*, *10*(7), 1431–1442. https://doi.org/10.5194/nhess-10-1431-2010

Chamberlain, C. J., Frank, W. B., Lanza, F., Townend, J., & Warren-Smith, E. (2021). Illuminating the pre-co-and post-seismic phases of the 2016 M7.8 Kaikōura earthquake with 10 years of seismicity. *Journal of Geophysical Research: Solid Earth*, *126*(8), e2021JB022304. https://doi.org/10.1029/2021JB022304

Clark, K., Nissen, E., Howarth, J., Hamling, I., Mountjoy, J., Ries, W., et al. (2017). Highly variable coastal deformation in the 2016 MW7.8 KaikÅura earthquake reflects rupture complexity along a transpressional plate boundary. *Earth and Planetary Science Letters*, *474*, 334–344. https://doi.org/10.1016/j.epsl.2017.06.048

Drob, D. P., Emmert, J. T., Meriwether, J. W., Makela, J. J., Doornbos, E., Conde, M., et al. (2015). An update to the Horizontal Wind Model (HWM): The quiet time thermosphere. *Earth and Space Science*, *2*(7), 301–319. https://doi.org/10.1002/2014EA000089

Georges, T. M., & Hooke, W. H. (1970). Wave-induced fluctuations in ionospheric electron content: A model indicating some observational biases. *Journal of Geophysical Research*, *75*(31), 6295–6308. https://doi.org/10.1029/JA075i031p06295

Hamling, I. J., Hreinsdóttir, S., Clark, K., Elliott, J., Liang, C., Fielding, E., et al. (2017). Complex multifault rupture during the 2016 Mw 7.8 Kaikoura earthquake, New Zealand. *Science*, *356*(6334). https://doi.org/10.1126/science.aam7194

Hannawald, P., Schmidt, C., Wüst, S., & Bittner, M. (2016). A fast SWIR imager for observations of transient features in OH airglow. *Atmospheric Measurement Techniques*, *9*(4), 1461–1472. https://doi.org/10.5194/amt-9-1461-2016

Hecht, J. H., Wan, K., Gelinas, L. J., Fritts, D. C., Walterscheid, R. L., Rudy, R. J., et al. (2014). The life cycle of instability features measured from the Andes Lidar observatory over Cerro Pachon on 24 March 2012. *Journal of Geophysical Research: Atmospheres*, *119*(14), 8872–8898. https://doi.org/10.1002/2014JD021726

Hines, C. O. (1960). Internal atmospheric gravity waves at ionospheric heights. *Canadian Journal of Physics*, *38*(11), 1441–1481. https://doi.org/10.1139/p60-150

Holden, C., Kaneko, Y., D'Anastasio, E., Benites, R., Fry, B., & Hamling, I. J. (2017). The 2016 Kaikōura earthquake revealed by kinematic source inversion and seismic wavefield simulations: Slow rupture propagation on a geometrically complex crustal fault network. *Geophysical Research Letters*, *44*(22), 11320–11328. https://doi.org/10.1002/2017GL075301

Inchin, P. A., Snively, J. B., Kaneko, Y., Zettergren, M. D., & Komjathy, A. (2021). Inferring the evolution of a large earthquake from its acoustic impacts on the ionosphere. *AGU Advances*, *2*(2), e2020AV000260. https://doi.org/10.1029/2020AV000260

Inchin, P. A., Snively, J. B., Williamson, A., Melgar, D., Aguilar Guerrero, J., & Zettergren, M. D. (2020). Mesopause airglow disturbances driven by nonlinear infrasonic acoustic waves generated by large earthquakes. *Journal of Geophysical Research: Space Physics*, *125*(6), e2019JA027628. https://doi.org/10.1029/2019JA027628

Inchin, P. A., Snively, J. B., Zettergren, M. D., Komjathy, A., Verkhoglyadova, O. P., & Tulasi Ram, S. (2020). Modeling of ionospheric responses to atmospheric acoustic and gravity waves driven by the 2015 Nepal 7.8 Gorkha earthquake. *Journal of Geophysical Research: Space Physics*, *125*(4), e2019JA027200. https://doi.org/10.1029/2019JA027200

Komatitsch, D., & Tromp, J. (1999). Introduction to the spectral element method for three-dimensional seismic wave propagation. *Geophysical Journal International*, *139*(3), 806–822. https://doi.org/10.1046/j.1365-246x.1999.00967.x

Komatitsch, D., & Vilotte, J.-P. (1998). The spectral element method: An efficient tool to simulate the seismic response of 2D and 3D geological structures. *Bulletin of the Seismological Society of America*, *88*(2), 368–392. https://doi.org/10.1785/BSSA0880020368

Le Dû, T., Simoneau, P., Keckhut, P., Hauchecorne, A., & Pichon, A. L. (2020). Investigation of infrasound signatures from microbaroms using oh airglow and ground-based microbarometers. *Advances in Space Research*, *65*(3), 902–908. https://doi.org/10.1016/j.asr.2019.11.026

Litchfield, N., Villamor, P., Dissen, R. V., Nicol, A. G. L., Barnes, P. M., Barrell, D. J. A., & Zinke, R. (2018). Surface rupture of multiple crustal faults in the 2016 Mw 7.8 Kaikōura, Earthquake, New Zealand. *Bulletin of the Seismological Society of America*, *8*(3B). https://doi.org/10.1785/0120170300

Makhlouf, U. B., Picard, R. H., & Winick, J. R. (1995). Photochemical-dynamical modeling of the measured response of airglow to gravity waves: 1. Basic model for OH airglow. *Journal of Geophysical Research*, *100*(D6), 11289–11311. https://doi.org/10.1029/94JD03327

Makhlouf, U. B., Picard, R. H., Winick, J. R., & Tuan, T. F. (1998). A model for the response of the atomic oxygen 557.7nm and the OH Meinel airglow to atmospheric gravity waves in a realistic atmosphere. *Journal of Geophysical Research*, *103*(D6), 6261–6269. https://doi.org/10.1029/97JD03082

Meng, X., Vergados, P., Komjathy, A., & Verkhoglyadova, O. (2019). Upper atmospheric responses to surface disturbances: An observational perspective. *Radio Science*, *54*(11), 1076–1098. https://doi.org/10.1029/2019RS006858

Pautet, P.-D., Taylor, M. J., Pendleton, W. R., Zhao, Y., Yuan, T., Esplin, R., & McLain, D. (2014). Advanced mesospheric temperature mapper for high-latitude airglow studies. *Applied Optics*, *53*(26), 5934–5943. https://doi.org/10.1364/AO.53.005934

Picone, J., Hedin, A. E., Drob, D. P., & Aikin, A. C. (2002). NRLMSISE-00 empirical model of the atmosphere: Statistical comparisons and scientific issues. *Journal of Geophysical Research*, *107*(A12), 15–16. https://doi.org/10.1029/2002JA009430

Pilger, C., Schmidt, C., Streicher, F., Wüst, S., & Bittner, M. (2013). Airglow observations of orographic, volcanic and meteorological infrasound signatures. *Journal of Atmospheric and Solar-Terrestrial Physics*, *104*, 55–66. https://doi.org/10.1016/j.jastp.2013.08.008

Press, F., & Harkrider, D. (1962). Propagation of acoustic-gravity waves in the atmosphere. *Journal of Geophysical Research*, *67*(10), 3889–3908. https://doi.org/10.1029/JZ067i010p03889

Sabatini, R., Marsden, O., Bailly, C., & Gainville, O. (2019). Three-dimensional direct numerical simulation of infrasound propagation in the earth's atmosphere. *Journal of Fluid Mechanics*, *859*, 754–789. https://doi.org/10.1017/jfm.2018.816

Savastano, G., Komjathy, A., Verkhoglyadova, O., Mazzoni, A., Crespi, M., Wei, Y., & Mannucci, A. J. (2017). Real-time detection of tsunami ionospheric disturbances with a stand-alone gnss receiver: A preliminary feasibility demonstration. *Nature*, *7*(1), 46607. https://doi.org/10.1038/srep46607

Schmidt, C., Höppner, K., & Bittner, M. (2013). A ground-based spectrometer equipped with an InGaAs array for routine observations of OH(3-1) rotational temperatures in the mesopause region. *Journal of Atmospheric and Solar-Terrestrial Physics*, *102*, 125–139. https://doi.org/10.1016/j.jastp.2013.05.001

Sedlak, R., Hannawald, P., Schmidt, C., Wüst, S., & Bittner, M. (2016). High-resolution observations of small-scale gravity waves and turbulence features in the OH airglow layer. *Atmospheric Measurement Techniques*, *9*(12), 5955–5963. https://doi.org/10.5194/amt-9-5955-2016

Snively, J. (2013). Mesospheric hydroxyl airglow signatures of acoustic and gravity waves generated by transient tropospheric forcing. *Geophysical Research Letters*, *40*(17), 4533–4537. https://doi.org/10.1002/grl.50886

Snively, J., Pasko, V. P., & Taylor, M. J. (2010). OH and OI airglow layer modulation by ducted short-period gravity waves: Effects of trapping altitude. *Journal of Geophysical Research*, *115*(A11), 0148–0227. https://doi.org/10.1029/2009JA015236

Tan, F., Ge, Z., Kao, H., & Nissen, E. (2019). Validation of the 3-D phase-weighted relative back projection technique and its application to the 2016 Mw 7.8 Kaikōura earthquake. *Geophysical Journal International*, *217*(1), 375–388. https://doi.org/10.1093/gji/ggz032

Ulrich, T., Gabriel, A.-A., Ampuero, J.-P., & Xu, W. (2019). Dynamic viability of the 2016 Mw 7.8 Kaikōura earthquake cascade on weak crustal faults. *Nature Communications*, *10*(1), 1213. https://doi.org/10.1038/s41467-019-09125-w

Wang, T., Wei, S., Shi, X., Qiu, Q., Li, L., Peng, D., et al. (2018). The 2016 Kaikoura earthquake: Simultaneous rupture of the subduction interface and overlying faults. *Earth and Planetary Science Letters*, *482*, 44–51. https://doi.org/10.1016/j.epsl.2017.10.056

Xu, W., Feng, G., Meng, L., Zhang, A., Ampuero, J. P., Bürgmann, R., & Fang, L. (2018). Transpressional rupture cascade of the 2016 Mw 7.8 kaikoura earthquake, New Zealand. *Journal of Geophysical Research: Solid Earth*, *123*(3), 2396–2409. https://doi.org/10.1002/2017JB015168

Zettergren, M., & Snively, J. (2015). Ionospheric response to infrasonic-acoustic waves generated by natural hazard events. *Journal of Geophysical Research*, *120*(9), 8002–8024. https://doi.org/10.1002/2015JA021116

Zhang, H., Koper, K. D., Pankow, K., & Ge, Z. (2017). Imaging the 2016 Mw 7.8 kaikoura, New Zealand, earthquake with teleseismic P waves: A cascading rupture across multiple faults. *Geophysical Research Letters*, *44*(10), 4790–4798. https://doi.org/10.1002/2017GL073461